# Nanocellulose-silver ensembles for ultrasensitive SERS: An investigation on the role of nanocellulose fibers in the generation of high-density hotspots

Kallayi Nabeela [a,b,1], Reny Thankam Thomas [a,1], A.P. Mohamed [a], Saju Pillai [a,b,*]

[a] *Functional Materials, Materials Science and Technology Division, CSIR-National Institute for Interdisciplinary Science and Technology (NIIST), Thiruvananthapuram, Kerala - 695 019, India*
[b] *Academy of Scientific and Innovative Research (AcSIR), Ghaziabad, Uttar Pradesh - 201 002, India*

## ARTICLE INFO

## ABSTRACT

Large scale hotspot engineering is a significant approach for the development of highly efficient surface enhanced Raman scattering (SERS) platforms. Herein, 2,2,6,6-tetramethylpiperidine-1-oxyl (TEMPO)-oxidized nanocellulose fiber (T-NCF) serves as a labyrinth for developing highly sensitive and stable silver-based SERS platform enabling single molecular level SERS detection of analytes. The SERS activity of 4-methylbenzenethiol (4-MBT) in silver nanoconstructs with dissimilar size and shape (denoted as Ag/NCF-I and Ag/NCF-II systems) synthesized by varying T-NCF to $Ag^+$ ratio, exhibited femtomolar sensitivity regardless of their structural variation. A detailed investigation of the SERS performance of both systems with 4-MBT at extremely low concentration ($10^{-15}$ M) is carried out with the help of large-area Raman intensity mapping in order to evaluate the role of T-NCF in Raman signal enhancement. The analytical enhancement factors (AEFs) for Ag/NCF-I and Ag/NCF-II are calculated to be $1.4 \times 10^{12}$ and $4.8 \times 10^{11}$, respectively. A mechanism of local enrichment of analytes is postulated anticipating the ability of flexible nanocellulose fibers to congregate AgNPs, resulting in induced plasmonic coupling of local electromagnetic fields and high-intensity hotspot generation. The potential of T-NCF in generating hotspots can be considered as an alternative strategy to develop standards with long-term colloidal stability and scale-up production of highly sensitive AgNP based plasmonic platforms. This investigation ascertains the potential of nanocellulose fibers in the development of a robust lithography-free SERS sensing platform with single molecule level sensitivity.

## 1. Introduction

The field of surface enhanced Raman scattering (SERS) has witnessed remarkable advances in the past few decades with a variety of approaches to upsurge the sensitivity of Raman analysis which relies on 'hotspots', where the electromagnetic fields are strongly confined. Since the existence of hotspots are known to be localized mostly within sharp edges [1], junctions [2,3], crevices [4], etc., research interests turned more towards the engineering of eccentric shapes [5,6] and cage structures [7] in nanodomains with the aim of concentrating electromagnetic field in constrained areas. However, the enhancement factor that could be achieved by controlling the shapes and size of plasmonic particles is limited to the extent of $10^5$ with respect to the Raman signals [8]. Therefore, hotspot engineering were often done by arranging these individual particles to dimers, trimers [9], arrays, different modes of assemblies [10] and superstructures [11] by precisely controlling the gap between plasmonic NPs [12,13] with the aid of aptamers [14], saline aggregating agents [15], modifying surfaces (e g., making it oleophobic or hydrophobic like in slippery liquid-infused porous surface-enhanced Raman scattering, SLIPSERS) [16], encased within silica shell or polymer matrix [17], etc. These approaches render the coupling of individual localized surface plasmon resonance (LSPR) bringing plasmonic structures within <2 nm proximity and thereby creating hotspots that lead to further increase in enhancement factors up to $10^8$ [8]. For instance, Xu et al. reported the use of aptamer/DNA to get the pyramid assembly of silver nanoparticles, enabling ultrasensitive detection of disease biomarkers [14].

High-density hotspot generation using polymeric systems is often acquired by embedding plasmonic NPs in the polymer ma-

* Corresponding author at: Functional Materials, Materials Science and Technology Division, CSIR-National Institute for Interdisciplinary Science and Technology (NIIST), Thiruvananthapuram, Kerala - 695 019, India.
*E-mail address:* pillai_saju@niist.res.in (S. Pillai).
[1] These authors contributed equally to this work.

trix that offers a cage-like environment capable of electrostatically, chemically, or mechanically trapping analytes which enable additional enhancement to SERS signals [18–21]. In this perspective, nanocellulose based plasmonic systems have recently emerged as a promising materials to develop highly sensitive SERS platforms [22–34]. Owing to its potential properties, nanocellulose fiber (NCF) based plasmonic system often fits the benchmark of an ideal SERS substrate in terms of sensitivity, stability, reproducibility and ease to scale up. The major highlights of nanocellulose based substrates are: 1) it is a naturally derived renewable and biodegradable material with minimal to no toxicity [31], 2) the carboxyl derivative of TEMPO-oxidized nanocellulose fiber (T-NCF) offers excellent anchoring sites for nucleation and growth of plasmonic NPs with surface roughness falling in SERS focal ranges [24,35], 3) unlike other polymeric materials which often compromise their sensitivity over the stabilizing effects due to the prevention of hotspots from being accessed by most analytes leading to suppressed SERS activity, NCFs with its low Raman background render the entry of probe molecule in the proximity of plasmonic NPs. Several groups have achieved a limit of detection (LOD) of probe molecules down to $10^{-9}$ M [22,23,26] and some of them permit single molecule SERS (SMSERS). For example, Kim et al. achieved SERS sensing of rhodamine 6G at LOD below 10 pM on flexible high-performance CNF/AuNP nanocomposite paper fabricated via simple vacuum infiltration [34]. However, a proper understanding of the theory behind the formation of high intense electromagnetic fields followed by huge signal amplification leads to SMSERS has not been fully understood. This is due to the challenges associated with the limited analysis and interpretation of single molecule events by poor statistics due to the limited occurrence of SMSERS signals [8].

Apart from the reports available explaining plasmonic coupling of well-defined nano assemblies like short linear arrays and aggregates of few particles, comprehensive studies on larger assemblies and superstructures are rare due to the difficulty in controlling their kinetics. Earlier, we have reported T-NCF as an ideal substrate for the growth of anisotropic silver nanoconstructs which exhibited exceptional stability and yielded high-performance SERS sensing [36]. In the present investigation, we studied the mechanism behind the role of T-NCF in exceptional enhancement of SERS signals creating additional hotspots enabling ultrasensitive detection of analytes falling in SMSERS regime. The SERS performance of two Ag/NCF systems, having dissimilar sizes and shapes, are investigated with large-area Raman mapping technique. Subsequently, a mechanism of local enrichment of hotspots by the preconcentration of analytes is also postulated.

## 2. Experimental section

### 2.1. Materials

Bio-extracted banana pseudo-stem fibers (BPSFs) were used for T-NCF extraction. Silver nitrate ($AgNO_3$), Sodium citrate tribasic dihydrate (TSC, $C_6H_5Na_3O_7 \cdot 2H_2O$), 4-methylbenzenethiol (4-MBT, $C_7H_8SO$) and methyl parathion ($C_{10}H_{14}NO_5PS$) were purchased from Sigma-Aldrich. Commercially available AgNP colloid (average size 60 nm) was purchased from Alfa Aesar. All the chemicals were used as received. Ultrapure deionized (DI) water of 18.2 MΩ•cm resistivity at 25 °C (Milli-Q purifier system, Merck, Germany) was used for preparing all standard solutions.

### 2.2. Characterizations

The morphological features of T-NCF and AgNPs were studied using atomic force microscopy (AFM) and transmission electron microscopy (TEM). AFM imaging was performed under tapping mode at room temperature (22 ±2°C) using MultiMode 8 atomic force microscope equipped with NanoScope V controller (Bruker, Santa Barbara, CA). Samples were prepared on ultra-smooth mica sheets. TEM images and corresponding energy-dispersive X-ray (EDX) analysis were obtained using FEI Tecnai 30 G2S-TWIN transmission electron microscope operated at an accelerating voltage of 300 kV. TEM sample preparation was done on the carbon-coated copper grid by drop-casting 2-3 drops of Ag/NCF colloid and dried at room temperature. The carboxyl content of T-NCF sample was calculated adopting the conductometric titration method [37,38]. X-Ray photoelectron spectra (XPS) were obtained using PHI 5000 VersaProbe II, ULVAC-PHI Inc., USA with monochromatic Al-Kα X-Ray source (hν = 1486.6 eV). Samples were prepared by drop-casting 10 μL of colloidal samples on a cleaned silicon substrate and dried under vacuum at ambient temperature. High-resolution spectra were acquired with pass energy, 46.95 eV and the spectra were deconvoluted using Multipak XPS data processing software (PHI Inc.). The binding energy was calibrated with respect to C1s peak at 284.8 eV. The plasmonic features of Ag colloids were studied using UV-Visible spectrophotometer (UV-2401PC, Shimadzu, Japan) in a 1 cm path-length quartz cell. Each Ag colloidal solution were diluted thrice prior to measurements. Colloidal stability was tested using Zeta potential measurements of colloids by dynamic light scattering with Nano ZS Malvern Instrument with no variation in concentrations and pH. The centrifugation of the as-prepared Ag/NCF colloids was done using Remi R-24 research centrifuge at 10000 rpm for 30 min. Ag content and subsequent yield of AgNPs in Ag/NCF colloid were estimated using inductively coupled plasma mass spectrometry (ICP-MS; Thermo Scientific iCAP-RQ).

### 2.3. SERS measurements

Raman spectra were collected using WI-Tec Raman microscope (WI-Tec, Inc., Germany, Alpha 300R) with a laser source of 633 nm wavelength; power - 2 mW; integration time - 2 s; lens - 20× objective; acquisition time - 2 s, accumulations - 10. The WI-Tec Project plus (version 4.1) software package was used for data interpretation. SERS spectra were collected after baseline correction. The Raman samples were prepared by mixing different concentrations of probe molecules with Ag colloids in 1:3 (v/v) ratio. 10 μL of the sample was drop-casted onto a clean glass slide and dried under vacuum at ambient temperature. SERS spectra were acquired at random spots. All experiments were conducted in triplicates.

The analytical enhancement factor (AEF) was estimated by the following equation.

$$AEF = \frac{I_{(SERS)} \times C_{(Raman)}}{I_{(Raman)} \times C_{(SERS)}}$$

$I_{(SERS)}$ is the intensity of SERS signal at LOD concentration $C_{(SERS)}$ of testing analyte. $I_{(Raman)}$ is the intensity of Raman signal of the same analyte and $C_{(Raman)}$ is the corresponding analyte concentration.

Focal volume of 20× objective was calculated using the equation,

Focal volume = 1.22/NA, where numerical aperture, NA=0.5 for 20×

### 2.4. Isolation of T-NCF

Preparation of T-NCF was done by subjecting purified banana pseudo-stem fibers (BPSF) to TEMPO mediated oxidation and subsequent ultra-sonication. A detailed procedure is given elsewhere [36].

### 2.5. Synthesis of Ag/NCF-I nanoconstructs

Flower-like Ag nanoconstructs were synthesized using modified Turkevich method which is discussed in our previous report [36]. The reduction of $Ag^+$ ions was carried out in the presence of T-NCF by the sequential addition of TSC.

### 2.6. Synthesis of Ag/NCF-II nanoconstructs

Adopting a slightly modified protocol we prepared Ag/NCF-II with initial $Ag^+$ ion concentration four times than the initial concentration of Ag/NCF-I. Initially, 1 mL of 0.5 wt% TSC was added to a boiling solution of 4 mM $AgNO_3$ (25 mL) previously dispersed with 1 wt% of T-NCF. After 5 min, the reaction mixture was diluted 4 times using DI water to reach a final T-NCF concentration of 0.25 wt%. The second batch of 1 mL of TSC (1 wt%) was then added to the boiling solution and kept heating for another 60 min. Dense yellow-colored Ag/NCF-II colloid was cooled immediately to prevent further reduction. The colloid was purified by dialyzing against DI water for 4 hours.

## 3. Results and discussion

### 3.1. Effect of T-NCF/Ag$^+$ ratio on the morphology of nanocellulose-silver ensemble

In the past few years, nanocellulose have been accepted as soft template or matrix in plasmonic NP synthesis along with its excellent capping and reducing actions. We prepared biomass-derived T-NCFs having width, $13\pm3$ nm and length, several hundreds of nanometer [36], by a TEMPO-mediated oxidation of holocellulose and subsequent defibrillation through ultrasonication. The fibrillar morphology of T-NCF thus obtained from BPSF is revealed from the AFM height image shown in S1, supporting information. It is well-known that the number of carboxyl groups contribute to the nucleation of zerovalent AgNPs. Therefore, T-NCFs with carboxyl content, ca. 1.27 mmol/g was utilized to prepare highly stable silver colloid (see S2, supporting information for stability studies), intercalated within T-NCF network under otherwise identical conditions. Exploiting the combined reducing and stabilizing actions of T-NCF and TSC, two types of Ag colloidal systems: one with hetero-shaped nanoconstruct termed as Ag/NCF-I and the other with homo-shaped nanoconstruct, Ag/NCF-II, were synthesized by varying the initial concentration of $Ag^+$ ions. The selection of two systems is made so as to distinguish the contribution of T-NCF from that of the structural features of colloidal particles towards plasmon enhanced sensing.

The morphological analysis of both systems is shown in Fig. 1. The TEM image of Ag/NCF-I (Fig. 1a) system exhibited flower-like AgNPs of size ranging from 200-600 nm together with a large number of tiny spherical AgNPs of size <5 nm. Whereas, the latter system (Fig. 1b) contains only spherical AgNPs with predominantly two size ranges, larger particles in 20-40 nm and smaller particles in <5 nm size ranges. Owing to the large scope for non-covalent interactions, flexible polymeric chains of T-NCF form entangled networks providing a perfect platform for further growth of plasmonic NPs. Serving as both reducing and stabilizing agent, T-NCF greatly restricts the coagulation of NPs soon after the formation of nuclei since it preferably happens at the carboxyl ends of oxidized NCFs. Fig. 2 illustrates the schematic of formation of silver nanoconstructs in presence of T-NCF (nanocellulose-silver ensemble) under different T-NCF to $Ag^+$ ratios.

A higher T-NCF to $Ag^+$ ratio in the reaction medium promotes aggregation of smaller AgNPs within the extended fiber network resulting in exceptionally stable colloid (zeta potential value, -69.4 mV [36]) of anisotropic AgNP assembly (Fig. 2a). Whereas, in the latter case (Fig. 2b), the number of $Ag^+$ ions available per T-NCF were four times higher than that of the former, resulted in the formation of a large number of Ag nuclei near T-NCFs in presence of additional reducing agent (TSC) present in the medium. The system therefore subsequently ends up in thermodynamically stable spherical NPs (zeta potential value, -52.5 mV). In our previous study, we demonstrated T-NCFs promote anisotropic growth only above 0.25% T-NCF concentration, below which only spherical or multi-twinned AgNPs (where no tiny satellite-like AgNPs are present) were found to form under the adopted preparation conditions [36].

Further, X-ray photoelectron spectroscopy (XPS) was used to understand the surface electronic features of the nanocellulose-silver ensembles. Fig. 3 shows the high-resolution deconvoluted spectra of Ag/NCF-I and Ag/NCF-II systems. The Ag3d line scans of Ag/NCF-I (Fig. 3a) and Ag/NCF-II (Fig. 3b) were further deconvoluted to Ag($3d_{5/2}$) and Ag($3d_{3/2}$) peaks centered at 368.2 eV 374.2 eV, respectively with a spine energy separation of 6 eV validates the formation of metallic Ag [39]. A noticeable additional shoulder peak was observed in Ag3d peaks of Ag/NCF-I centering at 369.4 eV (see Fig. 3a) which was found less intense in Ag/NCF-II. It is reported that the peaks at ~369.4 eV are indicative of the presence of sub-nano Ag particles or Ag clusters [40,41]. The peak position and broadness of this Ag cluster peak may vary based on the cluster size formed [42]. The above results suggest the presence of larger number of silver clusters in the former than the latter system. This observation indicates that these clusters may tend to ensemble towards Ag nanoconstructs where larger AgNPs were surrounded by tiny satellite-like nano and/or sub-nano Ag particles.

Further, for the quantification of AgNPs bound to T-NCF matrix, as-prepared colloids were centrifuged to remove larger particles followed by dialysis of supernatant, rendering the removal of unreacted $Ag^+$ ions as well as smaller free AgNPs. The ICP-MS studies revealed AgNPs yield of 89.9% and 75.6% for Ag/NCF-I and Ag/NCF-II systems, respectively. Another observation is that the Ag/NCF-I system showed no visible particles settled at the bottom upon centrifugation, which strongly hints that the larger flower-like Ag nanoconstructs formed are well stabilized in T-NCF network. Whereas, a fraction of 7.5% AgNPs were removed from the Ag/NCF-II colloid upon centrifugation, which is considered as the loosely bound NPs without the capping effect of T-NCF. Additionally, AFM images shed light on the role of T-NCF as a matrix providing anchoring sites for the growth of highly stable plasmonic NPs (supporting information, S3).

### 3.2. Plasmonic properties of nanocellulose-silver ensembles

The plasmonic characteristics of the colloids were studied using UV-Visible absorption spectroscopy, which confirmed the plasmonic band of AgNPs (Fig. 4a). The intense yellow color observed for Ag/NCF-II colloid (see Fig. 4a, inset photographs) indicates a higher concentration of AgNPs as compared to the other system. Generally, surface plasmon depends on size, shape and agglomeration state of plasmonic NPs. A shift in the resonance and the variation in its bandwidth are thus important parameters to characterize AgNPs. However, the broadness of the plasmonic peak depends upon the monodispersity of particles [43]. Interestingly, despite the large variation in size and morphology of the particles, plasmonic peaks show absorption maxima both centered at ~401 nm with slight broadness for Ag/NCF-I colloid as seen in the enlarged area of yellow dotted box marked in the spectra (see Fig. 4a, inset). This observation can be justified by the formation of larger anisotropic AgNPs as a result of controlled aggregation mechanism in the case of Ag/NCF-I [36]. This is supported by TEM image (Fig. 4b) obtained at the intermediate growth stage of flower-like Ag nanoconstruct showing smaller AgNPs grown over T-NCF matrix that sub-
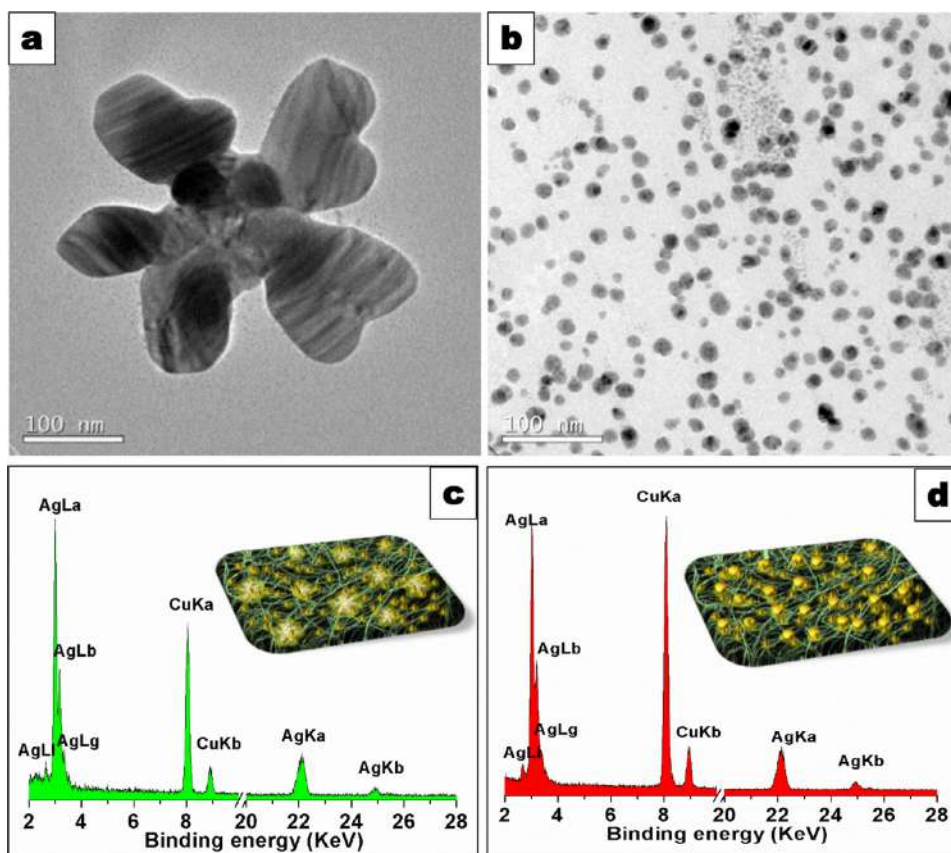
**Fig. 1.** TEM images of (a) Ag/NCF-I and (b) Ag/NCF-II. Corresponding EDX spectra (c) and (d) obtained for Ag/NCF-I and Ag/NCF-II, respectively. The inset cartoons show the representative distribution of nanostructures in the T-NCF matrix.
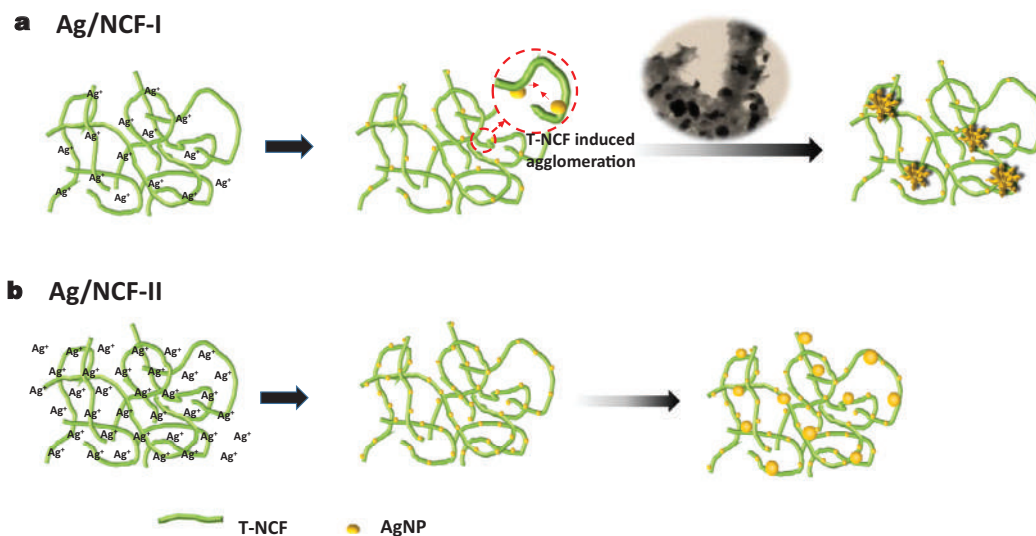


**Fig. 2.** Schematic illustration of (a) Ag/NCF-I and (b) Ag/NCF-II formation.

sequently grow into flower-like morphology. On the other hand, the presence of a higher T-NCF to Ag$^+$ ratio bring the as-formed AgNPs together by non-covalent interactions of T-NCFs resulting in the formation of anisotropic structures. However, the role of T-NCF restricted only to the capping and reducing action in Ag/NCF-II system yielding thermodynamically stable spherical structures attached to T-NCF matrix (TEM image is given in Fig. 4c). One would also expect that no more T-NCF were available to assemble NPs in the latter system.

### 3.3. SERS response

The SERS responses of Ag/NCF-I and Ag/NCF-II systems were investigated using 4-MBT, which is an ideal Raman reporter molecule that binds effectively with metals through thiol-linkage. Consistent with the low SERS cross-section of polysaccharides [29], we considered all SERS peaks observed were from the probe molecules alone. Thus, the SERS spectra acquired with Ag/NCF-I and Ag/NCF-II (Fig. 5a, spectra 1 and 2, respectively) for 10$^{-15}$ M dilution of
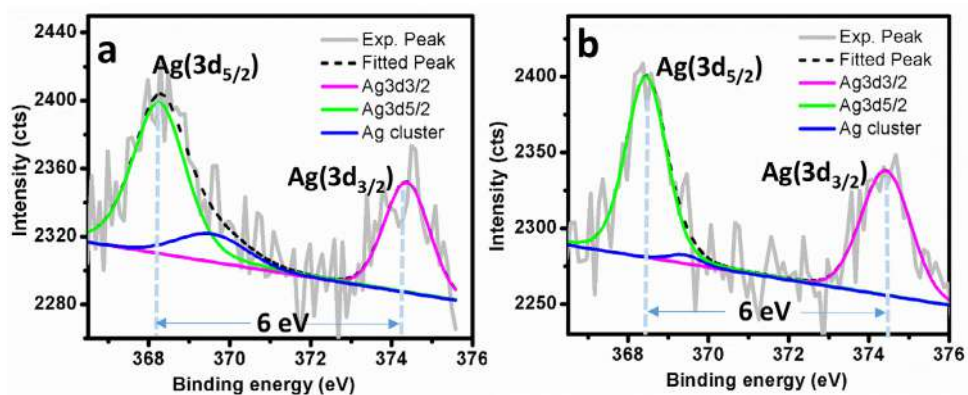
**Fig. 3.** XPS high-resolution spectra of Ag3d orbitals of (a) Ag/NCF-I and (b) Ag/NCF-II.
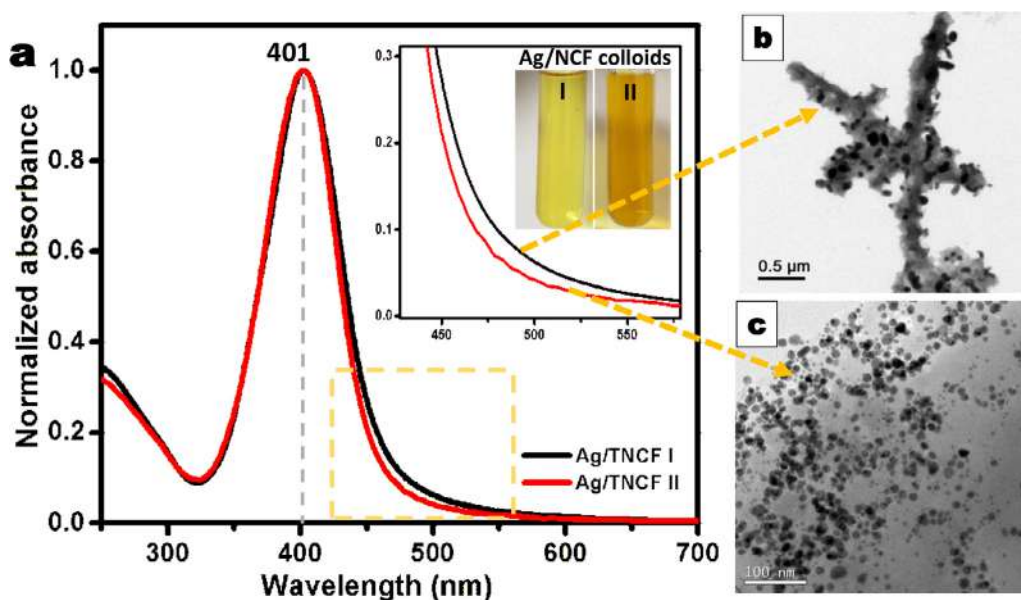


**Fig. 4.** (a) UV-Visible absorption spectra showing plasmonic peaks corresponding to Ag/NCF-I and Ag/NCF-II, inset shows magnified area of yellow dotted box revealing broadness in the spectra with photographs of both Ag/NCF colloidal systems, (b) the growth of AgNPs on T-NCFs taking anisotropic morphology with its networking effect, (c) Ag/NCF-II showing distribution of AgNPs all over the T-NCF matrix.
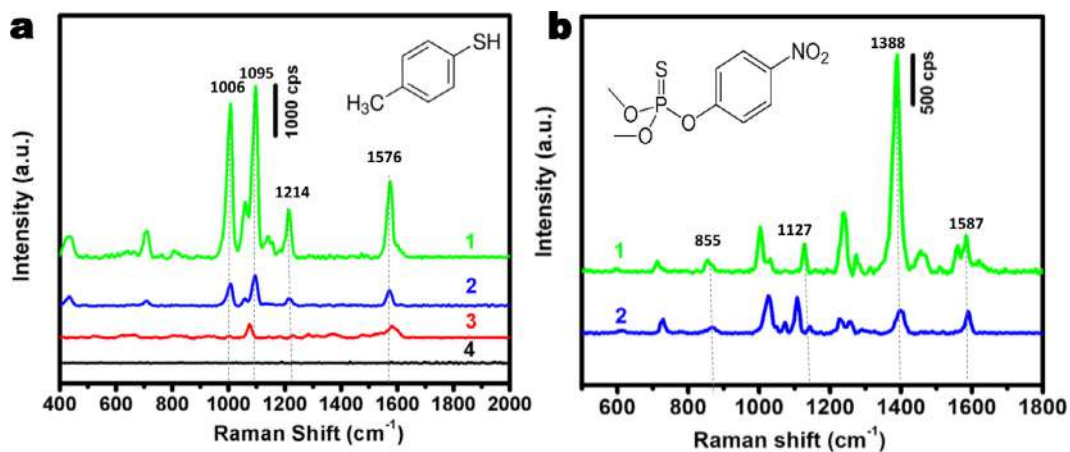


**Fig. 5.** (a) SERS spectra of 4-MBT at (1 $10^{-15}$ M concentration on Ag/NCF-I, (2 $10^{-15}$ M concentration on Ag/NCF-II, (3). $10^{-7}$ M concentration on standard spherical AgNPs and (4 Raman spectrum of 0.01 M 4-MBT. (b) SERS spectra acquired for methyl parathion ($10^{-15}$ M) on (1 Ag/NCF-I and 2 Ag/NCF-II.

4-MBT both show well-resolved characteristic bands at 1095 cm$^{-1}$, a combination of the phenyl ring breathing mode, C–H in-plane bending and C–S stretching; 1576 cm$^{-1}$, aromatic ring stretching, etc [44]. An AEF of $1.4 \times 10^{12}$ is calculated for Ag/NCF-I and $4.8 \times 10^{11}$ for Ag/NCF-II corresponding to the peak at 1095 cm$^{-1}$. We compared the above observation with a commercially available spherical AgNPs (with average size 60 nm) by acquiring SERS spectrum of $10^{-7}$ M concentration of 4-MBT (Fig. 5a, spectrum 3) and found that T-NCF based system is capable of yielding at least $10^8$ times SERS signal enhancement. In the control experiment, Raman spectrum of 0.01 M 4-MBT (Fig. 5a, spectrum 4) showed very weak signals. To explore the applicability of as-prepared SERS platforms in monitoring environmental organic pollutants, methyl parathion (a hazardous organophosphorous pesticide that has often been illegally overused to control sucking and chewing insects) was used as an analyte molecule. The results (see Fig. 5b) show that methyl parathion can be identified even when the concentration was lowered to femtomolar level, lower than the safety limits, with characteristic peaks assigned at 855 cm$^{-1}$, P-O stretching; 1127 cm$^{-1}$, C–N stretching; 1388 cm$^{-1}$, C-O bending; 1587 cm$^{-1}$, phenyl ring stretching [45].

### 3.4. SERS mapping

The above observations point that the excellent performance of Ag/NCF cannot be simply attributed to the intrinsic properties of the AgNPs, but rather involves both their favorable distribution in the T-NCF matrix. It is noteworthy that several pioneer groups have provided theoretical explanations for the generation of intense SERS signals acquired from various hybrid models of few particles of organized assemblies within the framework of plasmonic theory [10,46]. Nevertheless, a substantial foundation for the huge amplification of Raman signals of probe molecules from random arrangements or superstructures aroused by virtue of nanocellulose has not been given in this material point of view to the best of our knowledge. In fact, it is challenging to govern the contribution of SERS hotspots from the overall signals since the contribution from molecules outside the hotspots is unknown. Therefore, we look forward to a better explanation for the detection at a strikingly low abundance of analyte molecules in the presence of nanocellulose. In this aspect, it is necessary to fundamentally understand the distribution of analyte molecules over the substrate to reveal the mechanism behind enhanced SERS performance. Since single spectra acquisition gives information only for a small probe volume (~1.5 μm), we performed point-by-point wide-area ($25 \times 25 \ \mu m^2$) SERS mapping of 4-MBT/Ag colloid mixture with a concentration of $10^{-15}$ M 4-MBT at 633 nm with 150 measured spectra per line on T-NCF based SERS substrate. Uniform drying within the probe volume is essential in order to avoid the possible field effects that originated from uneven sample spreading. The uniform drying and sample distribution of the drop-casted 4-MBT/Ag colloid mixture on Ag/NCF-I and Ag/NCF-II were confirmed from the bright-field images Fig. 6a and 6d, which showed uniform distribution under $20 \times$ objective. Fig. 6b and 6e show the SERS intensity maps corresponding to the major signals present at 1000-1100 cm$^{-1}$ region taken from the specified $25 \times 25 \ \mu m^2$ areas (red dotted squares marked in respective bright-field images), giving the overview of SERS active zones. From Fig. 6b, it could be observed that the Raman mapping of 4-MBT on Ag/NCF-I features a throughout but inhomogeneous coverage of SERS active zones over the scanned area. Representative SERS single spectra from different spots marked in Fig. 6b are given in Fig. 6c, indicating small variation in SERS activity over the mapped region. However, the Raman map corresponding to Ag/NCF-II (Fig. 6e) shows more scattered and less probable distribution of high-density SERS active sites. Fig. 6f shows the corresponding SERS spectra of the marked hotspots in Fig. 6e. We observed that the detection at concentration down to $10^{-17}$ M (with AEF, $2.4 \times 10^{13}$) was still possible in Ag/NCF-I, but with poor reproducibility. The single spectra and corresponding SERS intensity mapping are given in S4, supporting information. Further decrease in concentration down to this level resulted in strongly fluctuating SERS signals, which might be due to the surface diffusion of analytes in and out of the hotspots, which accounts for the existence of single molecule events in SERS detection [47]. In fact, since very few molecules can be expected in an area of $25 \times 25 \ \mu m^2$, the uniform distribution of analyte molecules is not convincing. Therefore, an analyte enrichment mechanism has been postulated for the ultrasensitive detection of analyte molecules at concentrations down to femtomolar level due to the gathering effect of T-NCF to ensemble the nanostructures. The clustered distribution of SERS intensity observed in both cases testify the foregoing mechanism.

### 3.5. High-density hotspot formation

In principle, a surge in electromagnetic field intensity (hotspots generation) occurs when the NPs are brought in close proximity (usually <2nm) which resulted in the coupling of individual LSPR in a phenomenon referred to as plasmon hybridization or plasmon coupling. With a further reduction in gap below 1 nm, a sharp increase in field enhancement is observed [48]. Fig. 7a shows the schematic representation of a Raman active molecule that falls in a hotspot region between the gap of two plasmonic structures. In light of this electromagnetic gap theory, we can address the SM-SERS sensitivity observed for Ag/NCF platforms. The SERS intensity map discussed in the previous section strongly hints the inevitable role of T-NCF in increasing the sensitivity of the as-fabricated SERS substrate. In our previous report, we could justify the high sensitivity observed for Ag/NCF-I with the polarization of incident light by the anisotropic structures present in the system. However, it is worth mentioning that the latter system, Ag/NCF-II lacks any structural features like sharp edges, folds, corners, crevices, etc. that is capable of concentrating electromagnetic fields in confined areas, but still exhibits femtomolar level sensitivity. A possible explanation for this observation is that, similar to that of Ag/NCF-I, numerous tiny satellite AgNPs attached to T-NCF are present in the system surrounding larger spherical AgNPs contribute to the field enhancement. The TEM image is shown in Fig. 7b, reveals the capping action of T-NCF that preserves the tiny AgNPs in close proximity of larger AgNPs with inter-particle distance <1 nm sufficient enough to generate high-density electromagnetic field between the particles. A single analyte moiety falling in this region will therefore be capable of showing SERS signal with single molecular sensitivity [48]. Fig. 7c represents the schematic illustration of an analyte molecule of interest falling in and outside of the hotspot region of a typical Ag nanoconstruct formed in presence of T-NCFs. Apart from this, as T-NCFs naturally shrink in the drying process, the inter-particle distance between allied AgNPs tends to decrease as shown in the schematic, Fig. 7d. The consequent volume reduction of the material drives the embedded colloidal AgNPs close to each other with the strong electrostatic attraction of flexible T-NCFs due to the greater extent of hydrogen bonding. This promotes the coupling between their respective electromagnetic fields and therefore reflect in their resultant SERS signals. Besides, the close packing of AgNPs could increase the possibility of the analytes confined between the T-NCF layers to be detected by SERS. Furthermore, the electromagnetic field effects from individual NPs themselves contribute moreover less towards the total SERS intensity in the absence of hotspots, but their contribution is predicted to be relatively smaller.

In brief, the exceptional sensitivity achieved for Ag/NCF systems regardless of their particle shapes and excitation parameters could be attributed to the high-density hotspots formed via
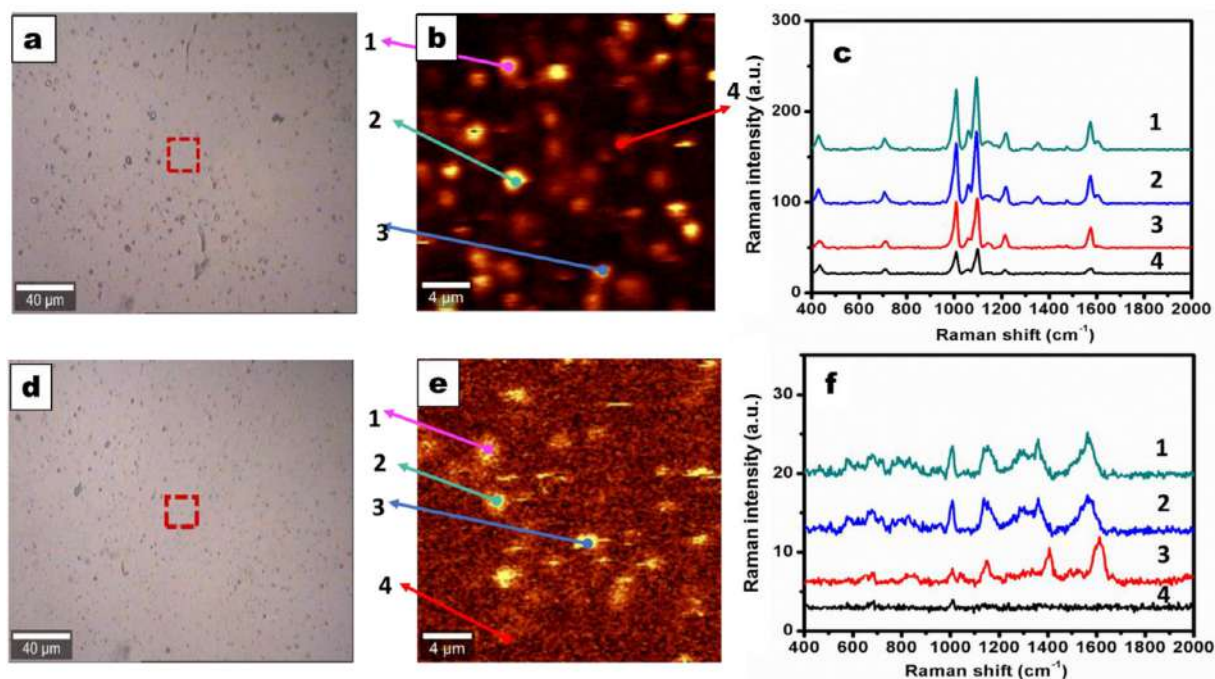
**Fig. 6.** The distribution of SERS intensity based on the substrate. Bright-field microscopic images (a) and (d) of $10^{-15}$ M 4-MBT drop-casted on Ag/NCF-I and Ag/NCF-II, respectively; (b) and (e): Corresponding XY intensity maps of SERS signals at 1000-1100 cm$^{-1}$ region from the area indicated by red dotted squares in a and d, respectively; (c) and (f): Representative SERS spectra obtained from selected areas marked in (b) and (e), respectively.
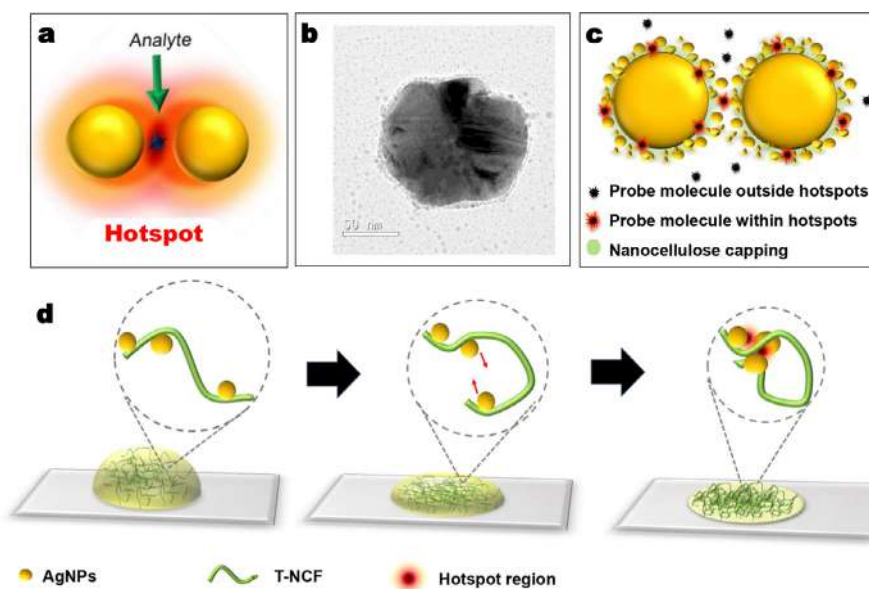


**Fig. 7.** (a) Schematic of hotspot formation between the gap of NPs, (b) representative TEM image of Ag/NCF system showing a pseudospherical AgNP surrounded by numerous tiny AgNPs trapped by T-NCF and corresponding schematic (c) showing probe molecules fall within and outside hotspot areas, (d) schematic showing drying induced shrinking of T-NCF and subsequent high-density hotspot formation between the allied AgNPs.

the formation of narrow-gap between the plasmonic structures introduced by the presence of flexible T-NCF in the system. Thus, the as-prepared T-NCF enabled SERS platform with a large number of high-density hotspots required neither well-defined nanostructures nor irreversible treatments like salt-induced aggregation to obtain strong signals. However, there are a variety of problems yet to overcome. The poor statistics of single molecular events at ultra-low concentration and related reproducibility issues need to be further tackled. Nevertheless, it is expected to inspire the SERS research to set-up a lithographic free low-cost and scalable route

for the development of efficient plasmonic sensing platforms with exceptional sensitivity and longer shelf-life.

## 4. Conclusion

In conclusion, we investigated the significant role of nanocellulose fibers in the SERS signal enhancement and found that the plasmonic silver nanoconstructs obtained using T-NCF were capable of yielding exceptional sensitivity compared to bare AgNPs. The unique role of T-NCF was revealed by the comparison of homo-shaped (spherical NPs with different sizes) Ag/NCF-I system with

hetero-shaped (anisotropic nanostructure surrounded with spherical particles) Ag/NCF-II system. Both systems were capable of generating consistently amplified SERS signals enabling femtomolar level detection of 4-MBT, achieving the limit of SMSERS. AEF values estimated for Ag/NCF-I and Ag/NCF-II were $1.4 \times 10^{12}$ and $4.8 \times 10^{11}$, respectively. Further, as-prepared nanocellulose-silver ensembles were employed to detect trace phenolic pollutants such as methyl parathion (an organophosphorous pesticide) with LOD $10^{-15}$ M. The SERS intensity mapping were done for 4-MBT at femtomolar concentration, revealing a local enrichment mechanism of analytes driven by nanocellulose-silver ensembles upon drying resulted in the formation of high-density hotspots responsible for exceptional sensitivity. Besides, a large contribution towards SM-SERS was also suggested to arise from the gaps ($< 2nm$) between tiny satellite AgNPs surrounding larger Ag nanostructures held by T-NCFs in both cases. Thus, the synthesis strategy proposed herein resulted in Ag colloids with long-term stability (over two years) and can be easily scaled-up with excellent shelf-life. Moreover, the findings provide scope to revolutionize the present scenario of hotspot engineering with the aid of nanocellulose-based SERS substrates. Further, this study can be extended to other functional nanostructures with tailored plasmonic properties for a broad range of applications.

## Declaration of Competing Interest

The authors declare that they have no known competing financial interests or personal relationships that could have appeared to influence the work reported in this paper.

## Acknowledgements

## References

[1] C. Wang, B. Liu, X. Dou, Silver nanotriangles-loaded filter paper for ultrasensitive SERS detection application benefited by interspacing of sharp edges, Sens. Actuators, B 231 (2016) 357–364.

[2] L. Chen, W. Liu, D. Shen, Y. Liu, Z. Zhou, X. Liang, W. Wan, All-optical tunable plasmonic nano-aggregations for surface enhanced raman scattering, Nanoscale 11 (2019) 13558–13566.

[3] N.H. Kim, W. Hwang, K. Baek, M.R. Rohman, J. Kim, H.W. Kim, J. Mun, S.Y. Lee, G. Yun, J. Murray, Smart SERS hot spots: single molecules can be positioned in a plasmonic nanojunction using host–guest chemistry, J. Am. Chem. Soc. 140 (2018) 4705–4711.

[4] S.-Y. Ding, J. Yi, J.-F. Li, B. Ren, D.-Y. Wu, R. Panneerselvam, Z.-Q. Tian, Nanostructure-based plasmon-enhanced Raman spectroscopy for surface analysis of materials, Nat. Rev. Mater. 1 (2016) 16021.

[5] L. Rodríguez-Lorenzo, R.A. Alvarez-Puebla, I. Pastoriza-Santos, S. Mazzucco, O. Stéphan, M. Kociak, L.M. Liz-Marzán, F.J. Garciá de Abajo, Zeptomol detection through controlled ultrasensitive surface-enhanced Raman scattering, J. Am. Chem. Soc. 131 (2009) 4616–4618.

[6] M.J. Mulvihill, X.Y. Ling, J. Henzie, P. Yang, Anisotropic etching of silver nanoparticles for plasmonic structures capable of single-particle SERS, J. Am. Chem. Soc. 132 (2009) 268–274.

[7] K. Liu, Y. Bai, L. Zhang, Z. Yang, Q. Fan, H. Zheng, Y. Yin, C. Gao, Porous Au–Ag nanospheres with high-density and highly accessible hotspots for SERS analysis, Nano Lett 16 (2016) 3675–3681.

[8] M.D. Sonntag, J.M. Klingsporn, A.B. Zrimsek, B. Sharma, L.K. Ruvuna, R.P. Van Duyne, Molecular plasmonics for nanoscale spectroscopy, Chem. Soc. Rev. 43 (2014) 1230–1247.

[9] K.L. Wustholz, A.-I. Henry, J.M. McMahon, R.G. Freeman, N. Valley, M.E. Piotti, M.J. Natan, G.C. Schatz, R.P. Van Duyne, Structure– activity relationships in gold nanoparticle dimers and trimers for surface-enhanced Raman spectroscopy, J. Am. Chem. Soc. 132 (2010) 10903–10910.

[10] R. Thomas, R. Swathi, Linear and polygonal assemblies of plasmonic nanoparticles: incident light polarization dictates hot spots, J. Phy. Chem. C 120 (2016) 18733–18740.

[11] N. Gandra, A. Abbas, L. Tian, S. Singamaneni, Plasmonic planet–satellite analogues: hierarchical self-assembly of gold nanostructures, Nano Lett 12 (2012) 2645–2651.

[12] D.-K. Lim, K.-S. Jeon, H.M. Kim, J.-M. Nam, Y.D. Suh, Nanogap-engineereable raman-active nanodumbbells for single-molecule detection, Nat. Mater. 9 (2010) 60.

[13] J. Kumar, R. Thomas, R. Swathi, K.G. Thomas, Au nanorod quartets and Raman signal enhancement: towards the design of plasmonic platforms, Nanoscale 6 (2014) 10454–10459.

[14] L. Xu, W. Yan, W. Ma, H. Kuang, X. Wu, L. Liu, Y. Zhao, L. Wang, C. Xu, SERS encoded silver pyramids for attomolar detection of multiplexed disease biomarkers, Adv. Mater. 27 (2015) 1706–1711.

[15] M.Y. Chan, W. Leng, P.J. Vikesland, Surface-enhanced raman spectroscopy characterization of salt-induced aggregation of gold nanoparticles, ChemPhysChem 19 (2018) 24–28.

[16] S. Yang, X. Dai, B.B. Stogin, T.-S. Wong, Ultrasensitive surface-enhanced Raman scattering detection in common fluids, Proc. Natl. Acad. Sci. 113 (2016) 268–273.

[17] X. Xia, W. Li, Y. Zhang, Y. Xia, Silica-coated dimers of silver nanospheres as surface-enhanced Raman scattering tags for imaging cancer cells, Interface focus 3 (2013) 20120092.

[18] P. Aldeanueva-Potel, E. Faoucher, R.n.A. Alvarez-Puebla, L.M. Liz-Marzán, M. Brust, Recyclable molecular trapping and SERS detection in silver-loaded agarose gels with dynamic hot spots, Anal. Chem. 81 (2009) 9233–9238.

[19] R. Contreras-Cáceres, S. Abalde-Cela, P. Guardia-Girós, A. Fernández-Barbero, J. Pérez-Juste, R.A. Alvarez-Puebla, L.M. Liz-Marzán, Multifunctional microgel magnetic/optical traps for SERS ultradetection, Langmuir 27 (2011) 4520–4525.

[20] C.L. Zhang, K.P. Lv, H.P. Cong, S.H. Yu, Controlled Assemblies of Gold Nanorods in PVA Nanofiber Matrix as Flexible Free-Standing SERS Substrates by Electrospinning, Small 8 (2012) 648–653.

[21] P.P. Veerabaghu, P. Ramasamy, V. Sathe, A. Ramasamy, U. Mahalingam, Plasmonic silver nanospheres embedded $\varepsilon$-caprolactone/reduced graphite oxide nanolayers as active SERS substrates, Mater. Sci. Eng. C 101 (2019) 431–437.

[22] Y. Lu, Y. Luo, Z. Lin, J. Huang, A silver-nanoparticle/cellulose-nanofiber composite as a highly effective substrate for surface-enhanced Raman spectroscopy, Beilstein J. Nanotechnol. 10 (2019) 1270–1279.

[23] K. Oh, M. Lee, S.G. Lee, D.H. Jung, H.L. Lee, Cellulose nanofibrils coated paper substrate to detect trace molecules using surface-enhanced Raman scattering, Cellulose 25 (2018) 3339–3350.

[24] L. Zhang, X. Li, L. Ong, R.F. Tabor, B.A. Bowen, A.I. Fernando, A. Nilghaz, G. Garnier, S.L. Gras, X Wang, Cellulose nanofibre textured SERS substrate, Colloids Surf., A 468 (2015) 309–314.

[25] H. Wei, P.J. Vikesland, pH-triggered molecular alignment for reproducible SERS detection via an AuNP/nanocellulose platform, Sci. Rep. 5 (2015) 18131.

[26] L. Tian, J. Luan, K.-K. Liu, Q. Jiang, S. Tadepalli, M.K. Gupta, R.R. Naik, S. Singamaneni, Plasmonic biofoam: a versatile optically active material, Nano Lett. 16 (2015) 609–616.

[27] J.E. Villa, D.P. Dos Santos, R.J. Poppi, Fabrication of gold nanoparticle-coated paper and its use as a sensitive substrate for quantitative SERS analysis, Microchim. Acta 183 (2016) 2745–2752.

[28] Z. Xiong, M. Lin, H. Lin, M. Huang, Facile synthesis of cellulose nanofiber nanocomposite as a SERS substrate for detection of thiram in juice, Carbohydr. Polym. 189 (2018) 79–86.

[29] S. Zhang, R. Xiong, M.A. Mahmoud, E.N. Quigley, H. Chang, M. El-Sayed, V.V. Tsukruk, Dual-excitation nanocellulose plasmonic membranes for molecular and cellular SERS detection, ACS Appl. Mater. Interfaces 10 (2018) 18380–18389.

[30] C.H. Lee, L. Tian, S. Singamaneni, based SERS swab for rapid trace detection on real-world surfaces, ACS Appl. Mater. Interfaces 2 (2010) 3429–3435.

[31] L. Tian, Q. Jiang, K.K. Liu, J. Luan, R.R. Naik, S. Singamaneni, Bacterial nanocellulose-based flexible surface enhanced raman scattering substrate, Adv. Mater. Interfaces 3 (2016) 1600214.

[32] M. Park, H. Chang, D.H. Jeong, J. Hyun, Spatial deformation of nanocellulose hydrogel enhances SERS, BioChip J. 7 (2013) 234–241.

[33] P. Liou, F.X. Nayigiziki, F. Kong, A. Mustapha, M. Lin, Cellulose nanofibers coated with silver nanoparticles as a SERS platform for detection of pesticides in apples, Carbohydr. Polym. 157 (2017) 643–650.

[34] D. Kim, Y. Ko, G. Kwon, Y.-M. Choo, J. You, Low-cost, high-performance plasmonic nanocomposites for hazardous chemical detection using surface enhanced Raman scattering, Sens. Actuators, B 274 (2018) 30–36.

[35] J. Van Rie, W. Thielemans, Cellulose–gold nanoparticle hybrid materials, Nanoscale 9 (2017) 8525–8554.

[36] K. Nabeela, R.T. Thomas, J.B. Nair, K.K. Maiti, K.G.K. Warrier, S. Pillai, TEMPO-Oxidized nanocellulose fiber-directed stable aqueous suspension of plasmonic flower-like silver nanoconstructs for ultra-trace detection of analytes, ACS Appl. Mater. Interfaces 8 (2016) 29242–29251.

[37] R. Shinoda, T. Saito, Y. Okita, A. Isogai, Relationship between length and degree of polymerization of TEMPO-oxidized cellulose nanofibrils, Biomacromolecules 13 (2012) 842–849.

[38] T. Saito, A. Isogai, TEMPO-mediated oxidation of native cellulose. The effect of oxidation conditions on chemical and crystal structures of the water-insoluble fractions, Biomacromolecules 5 (2004) 1983–1989.

[39] T. Jiao, H. Guo, Q. Zhang, Q. Peng, Y. Tang, X. Yan, B. Li, Reduced graphene oxide-based silver nanoparticle-containing composite hydrogel as highly efficient dye catalysts for wastewater treatment, Sci. Rep. 5 (2015) 11873.

[40] B.-H. Mao, R. Chang, L. Shi, Q.-Q. Zhuo, S. Rani, X.-S. Liu, E.C. Tyo, S. Vajda, S.-D. Wang, Z. Liu, A near ambient pressure XPS study of subnanometer silver clusters on $Al_2O_3$ and $TiO_2$ ultrathin film supports, Phys. Chem. Chem. Phys. 16 (2014) 26645–26652.

[41] J.N. O'Shea, J. Schnadt, S. Andersson, L. Patthey, S. Rost, A. Giertz, B. Brena, J.-O. Forsell, A. Sandell, O. Björneholm, X-ray photoelectron spectroscopy of low surface concentration mass-selected Ag clusters, J. Chem. Phys. 113 (2000) 9233–9238.

[42] R.E. Galindo, N. Benito, C. Palacio, A. Cavaleiro, S. Carvalho, Ag+ release inhibition from ZrCN–Ag coatings by surface agglomeration mechanism: structural characterization, J. Phys. D: Appl. Phys. 46 (2013) 325303.

[43] C. Noguez, Surface plasmons on metal nanoparticles: the influence of shape and physical environment, J. Phys. Chem. C 111 (2007) 3806–3819.

[44] R. Wang, X.-R. Shen, M. Zhang, R. Devasenathipathy, R. Pang, D.-Y. Wu, J. Zhang, J. Ulstrup, Z.-Q. Tian, Adsorption, chemical enhancement, and low–lying excited states of p-methylbenzenethiol on silver and gold nanoparticle surfaces: a surface enhanced raman spectroscopy and density functional theory study, J. Phys. Chem. C 123 (2019) 23026–23036.

[45] P. Wang, L. Wu, Z. Lu, Q. Li, W. Yin, F. Ding, H. Han, Gecko-inspired nanotentacle surface-enhanced Raman spectroscopy substrate for sampling and reliable detection of pesticide residues in fruits and vegetables, Anal. Chem. 89 (2017) 2424–2431.

[46] R. Thomas, R. Swathi, Organization of metal nanoparticles for surface-enhanced spectroscopy: a difference in size matters, J. Phys. Chem. C 116 (2012) 21982–21991.

[47] S.R. Emory, R.A. Jensen, T. Wenda, M. Han, S. Nie, Re-examining the origins of spectral blinking in single-molecule and single-nanoparticle SERS, Faraday Discuss 132 (2006) 249–259.

[48] L. Tong, H. Xu, M. Käll, Nanogaps for SERS applications, MRS Bull. 39 (2014) 163–168.